CDF/PHYS/ELECTROWEAK/PUBLIC/10864

Search for $ZW + ZZ \to \ell^+\ell^- + jj$ production at $\sqrt{s} = 1.96$ TeV

The CDF Collaboration[1]

[1] *http://www-cdf.fnal.gov*

(Dated: June 18, 2012)

Abstract

Diboson production where WW is a significant component has been observed at the Tevatron collider in semi-hadronic decay modes. We present a measurement of the cross section of ZW and ZZ production in the dilepton + dijet final state using 8.9 fb^{-1} of data recorded with the CDF detector at the Tevatron. We select events by identifying those that contain two charged leptons with a reconstructed invariant mass near the mass of the Z boson, two hadronic jets, and low transverse missing energy ($\not\!\!E_T$). We increase our sensitivity to $W/Z \to q\bar{q}'$ decays using a quark-gluon neural network discriminant that quantizes the spatial spread of the energy and track momenta contained within a jet. The number of signal events is extracted through a simultaneous fit to the dijet mass spectrum in three channels: a heavy-flavor tagged channel, a light-flavor tagged channel, and an untagged channel. We measure $\sigma_{ZW/ZZ} = 2.5^{+2.0}_{-1.0}$ pb, below but consistent with the SM cross section of ~ 5.08 pb. We establish a limit on the cross section of $\sigma_{ZW/ZZ} < 6.35$ pb at 95% CL.

I. INTRODUCTION

The standard model (SM) offers precise predictions for the production rates for self-interactions of the gauge bosons [1]. Differences between these predictions and measured diboson production cross sections may indicate the presence of new physics [2, 3], specifically in hadronic final states [4]. Additionally, since hadronic final states in diboson production are similar to associated Higgs boson production ($p\bar{p} \rightarrow VH + X$ where V=W, Z), the analysis techniques used to measure diboson production in partially hadronic final states are relevant to Higgs boson searches.

Measurements of diboson production are typically difficult to carry out due to the very small production cross sections of these processes, on the order of 10 pb or less [1]. Furthermore, measurements of decay channels where one W or Z boson decays hadronically are particularly challenging: while they have higher expected event yields than purely leptonic decay channels due to the higher $W/Z \rightarrow q\bar{q}'$ branching ratio, they also much higher expected backgrounds from QCD multi-jet processes and W/Z + jets events. Experiments at the Tevatron have previously measured the production of two gauge bosons in partially hadronic decay channels [5–8], but each of these measurements have included sensitivity to WW production, which has a higher cross section than ZW and ZZ production. Searches using b-tagging to increase sensitivity to events with $Z \rightarrow b\bar{b}$ decays have been conducted [9], but have not yet observed WZ/ZZ production in partially hadronic decay channels.

We present a measurement of the cross section of ZW/ZZ production in a final state with two leptons and at least two jets. We require the two leptons to be from the decay of a Z boson, and search for associated $W/Z \rightarrow q\bar{q}'$ decays by performing a fit to the dijet invariant mass (m_{jj}) spectrum. To maximize our sensitivity to diboson production, we separate events into three channels: a heavy-flavor tagged channel, largely sensitive to $ZZ \rightarrow \ell^+\ell^- b\bar{b}$ decays; a light-flavor tagged channel which utilizes a new artificial neural-network (ANN)-based discriminant that separates quark jets from gluon jets; and an "untagged" channel which contains the remaining events that pass our pre-selection requirements. The fit to the m_{jj} spectrum is performed simultaneously across these three channels.

II. THE CDF DETECTOR

The CDF II detector is described in detail elsewhere [10]. The detector is cylindrically symmetric around the proton beam line [11]. Tracking detectors are installed around the interaction point, and reconstruct the trajectories of charged particles. The tracking systems sit within a superconducting solenoid which produces a 1.4 T magnetic field aligned coaxially with the $p\overline{p}$ beams. Around the outside of the solenoid, calorimeter modules arranged in a projective tower geometry measure the energies of charged and neutral particles. A series of drift chambers sit outside the calorimeter, and are used to detect muons, which typically leave little energy in the calorimeter.

The Central Outer Tracker (COT) is a 3.1 m long open cell drift chamber which performs 96 track measurements in the region between 0.40 and 1.37 m from the beam axis, providing coverage in the pseudorapidity region $|\eta| \leq 1.0$. Sense wires are arranged in eight alternating axial and $\pm$ 2° stereo "superlayers" with 12 wires each. The position resolution of a single drift time measurement is about 140 μm. A five-layer double-sided silicon microstrip detector (SVX) covers the region between 2.5 to 11 cm from the beam axis. Three separate SVX barrel modules along the beam line cover a length of 96 cm, approximately 90% of the luminous beam interaction region. Three of the five layers combine an r-ϕ measurement on one side and a 90° stereo measurement on the other, and the remaining two layers combine an r-ϕ measurement with a small angle ($\pm$1.2°) stereo measurement. The typical silicon hit resolution is 11 μm. Additional Intermedia Silicon Layers (ISL) at radii between 19 and 30 cm from the beam line in the central region link tracks in the COT to hits in the SVX. The fiducial range of the silicon detector extends to $|\eta| \leq 2.0$.

Calorimeter modules sit outside the central tracking volume and solenoid. The inner electromagnetic layers consists of lead sheets interspersed with scintillator, while the outer hadronic layers consist of scintillators sandwiched between steel sheets. The calorimeter is split between central barrel ($|\eta| \leq 1.0$) and forward end plug ($1.1 \leq |\eta| \leq 3.64$) sections. Individual towers in central barrel subtend 0.1 in $|\eta|$ and 15° in ϕ. The sizes of the towers in the end plug calorimeter vary with $|\eta|$: subtending 0.1 in $|\eta|$ and 7.5° in ϕ at $|\eta| = 1.1$, and 0.5 in $|\eta|$ and 15° in ϕ at $|\eta| = 3.6$.

High-momentum jets, photons, and electrons leave isolated energy deposits in contiguous groups of calorimeter towers which can be summed together into an energy cluster. Electrons

are identified as isolated, mostly electromagnetic clusters, and quality cuts may be placed on the presence of a high-p_T track matched to the cluster. Jets are identified as electromagnetic and hadronic clusters with an electromagnetic fraction $\frac{E_{EM}}{E_{total}} = \frac{E_{EM}}{E_{EM}+E_{had}} \leq 0.9$, clustered using the JETCLU cone algorithm [12] with a fixed cone size of $R = \sqrt{\eta^2 + \phi^2} = 0.4$.

Outside the calorimeters, a collection of drift chambers detect muons. A four-layer stack of planar drift chamber detects muons with $p_T > 1.4$ GeV/c, and another four layers of drift chambers behind 60 cm of steel detects muons with $p_T > 2.0$ GeV/c. Both systems cover a region of $|\eta| \leq 0.6$, though they have different structure and their geometrical coverages do not overlap exactly. Muons in the region between $0.6 \leq |\eta| \leq 1.0$ pass through at least four drift layers lying in a conic section outside of the central calorimeter. Muons may be identified as either COT tracks that extrapolate to hits on the muon detectors, or isolated tracks unmatched to hits in the muon detectors, but with tighter tracking quality requirements.

III. DATASET AND EVENT SELECTION

We analyze the full dataset of $p\overline{p}$ collisions collected by the CDF II detector. We require events to be from periods where the calorimeter, muon detectors, and silicon detectors were all functioning properly, corresponding to an integrated luminosity of 8.9 fb^{-1}. Events are selected via a suite of high-p_T electron and muon triggers, the bulk of which require at least one lepton with $p_T > 18$ GeV/c. We require events contain two electrons or two muons with $p_T \geq 20$ GeV/c, and we calculate the trigger and reconstruction efficiencies by comparing data and Monte Carlo simulation in a $Z \to \ell\ell + 1$ jet ($E_T > 20$ GeV) selection.

For the final analysis, we select events with two leptons, and two or more jets. In addition to the p_T requirements on the leptons, we require leptons with well-reconstructed tracks to be of opposite charge, and that the reconstructed dilepton invariant mass, $m_{\ell\ell}$, be consistent with the mass of the Z boson: 76 GeV/$c^2 \leq m_{\ell\ell} \leq$ 106 GeV/c^2. We require both leading-E_T jets have $E_T > 25$ GeV and $|\eta| \leq 2.0$, and not be matched within $\Delta R \leq 0.4$ to a reconstructed lepton. Additionally, the two jets must be separated with $\Delta R \geq 0.7$. Finally, as our final state should contain no objects that fail to be reconstructed in the detector, we also require the missing transverse energy, $\not\!\!E_T$ [13], be less than 20 GeV.

After this selection, we have three major sources of backgrounds. Our dominant back-

ground comes from production of a Z boson which decays to an e^+e^- or $\mu^+\mu^-$ pair, produced in association with two jets. Monte Carlo (MC) simulations generated using ALPGEN [14] as an event generator interface with PYTHIA [15] for showering are used to estimate this background. The contributions from $Z + b\bar{b}$ processes are enhanced, in order to agree with measurements [16].

Another significant background results from jets misidentified as leptons. The contributions from these lepton "fakes" are estimated via a data-driven method, but this method is different for muons and electrons. For the former, we use events with same-sign muon pairs (rather than opposite-sign) that otherwise satisfy all of our event selection requirements. For the latter, we construct a "fake rate", representing the likelihood a jet fakes an electron, as a function of jet E_T and η using jet-triggered data that has few "real" electrons. This fake rate is then applied to e-jet pairs in the high-p_T electron dataset, where the jet is then treated as a second electron, and the event selection requirements are otherwise normally applied.

While the cut on $\not\!\!E_T$ reduces its total contribution, top quark pair production, where each top quark decays into a leptonic final state ($t \to Wb \to \ell\nu_\ell b$), may appear in our final selection, especially in our heavy-flavor tagged region. We estimate $t\bar{t}$ contributions using PYTHIA. Finally, our ZW and ZZ signal samples are also estimated using PYTHIA.

IV. JET ENERGY CALIBRATION

The jets used in this analysis have their energy as measured by the calorimeter corrected for a number of effects that distort the true jet energy. These effects include consistency across $|\eta|$ and time, contributions from multiple $p\overline{p}$ interactions per beam crossing (pileup) and the underlying event, the non-linear response of the calorimeter, and energy radiated outside of the jet cone. The jet energy scale (JES) corrections applied are described in great detail in [17].

These energy corrections, however, do not distinguish between the response of gluon and quark jets. The largest energy corrections, which correct the energy scale of calorimeter jets to better match that of particle jets and the initial parton energy, are derived using PYTHIA [15] dijet Monte Carlo simulations (MC). Differences in the response of gluon and quark jets between MC and data may lead to differences in the measured energies of these

objects that are not covered by the systematic uncertainties on the JES.

It is possible to derive a correction for the response of quark and gluon jets in data and MC given two independent samples of jets, with different quark fractions, balanced against objects of known energy. We use events where a jet balances with a γ, which are rich in quarks, and utilize the significant number of $Z \to \ell^+\ell^-+$ jet events now available, which are more rich in gluons. We construct the balance of the jet with these better measured reference objects:

$$K_{Z/\gamma} = ({E_T}^{\rm jet}/p_T^{Z/\gamma}) - 1 \tag{1}$$

. For well-measured jets, $K_{z/\gamma} = 0$. Rather than derive full and separate JES corrections for quark and gluon jets in data and MC, we compare the balance in data and MC and derive an additional correction to be applied to MC jets, based upon whether they are matched to quarks or gluons.

A. Dataset and Event Selection

The datasets and event selection for Z-jet balancing sample follow that described in Sec. III. We require two leptons consistent with being from the decay of a Z, and require events have one and only one jet with (uncorrected) $E_T > 3$ GeV within $|\eta| \leq 2.4$. Additionally, we ensure that the Z and jet are back-to-back by requiring the $\Delta\phi$ between the two objects be > 2.8 radians, and require $p_T^Z > 10$ GeV/c.

For the γ-jet balancing sample, we closely mirror the selection requirements described in [17]. We use events collected with an isolated central photon trigger covering the same data period as that of the high-p_T lepton samples. We compare this data to MC generated using PYTHIA for both $\gamma+$ jet, and also use PYTHIA MC samples to estimate the contributions from dijet production that contaminate our γ-jet balancing sample.

In order to avoid trigger biases, we require $E_T^\gamma > 27$ GeV and $0.2 \leq |\eta_\gamma| \leq 0.6$ in both data and MC. To decrease the contribution from dijet production, where a jet mimics our photon selection, we require the energy in the calorimeter and momentum in the tracking system contained within a cone of $R = 0.4$ around the photon to be less than 1 GeV and 2 GeV/c, respectively. As in the Z-jet balancing sample, we require events have one and only one jet with (uncorrected) $E_T > 3$ GeV within $|\eta| \leq 2.4$, and demand the $\Delta\phi$ between the jet and photon be > 3.0 radians. We further reduce contamination of our sample by vetoing

events with large pileup (more than 1 reconstructed interaction point), and by removing events with $\not\!\!E_T/E_T^\gamma > 0.8$, which likely contain activity from cosmic rays.

B. Determination of Correction

We can derive separate corrections for the quark and gluon jet energy scale in data and MC simulation using our Z-jet and γ-jet balancing samples in the following way. Suppose K_Z and K_γ are the necessary corrections to jet energies in the Z-jet and γ-jet balancing samples. Each correction should be a weighted average of separate corrections for quark and gluon jets: K_q and K_g, respectively. If $F_X^{q/g}$ is the quark/gluon fraction in sample X, then we can write:

$$K_Z = F_Z^q K_q + F_Z^g K_g = F_Z^q K_q + (1 - F_Z^q) K_g \tag{2}$$

$$K_\gamma = F_\gamma^q K_q + F_\gamma^g K_g = F_\gamma^q K_q + (1 - F_\gamma^q) K_g \tag{3}$$

These equations can be rewritten, solving for K_q and K_g:

$$K_q = \frac{1}{F_\gamma^q - F_Z^q}[(1 - F_Z^q)K_\gamma - (1 - F_\gamma^q)K_Z] \tag{4}$$

$$K_g = \frac{1}{F_\gamma^q - F_Z^q}[F_\gamma^q K_Z - F_Z^q K_\gamma] \tag{5}$$

These equations may be written separately for data and MC (thus with distinct ${K_X}^{\rm data}$ and ${K_X}^{\rm MC}$), and may include a dependence on the energy of the jet ($F_X^q \to F_X^q({E_T}^{\rm jet})$ and $K_X \to K_X({E_T}^{\rm jet})$).

Thus, in order to solve for K_q and K_g, we need $K_{Z/\gamma}$ and $F_{Z/\gamma}^q$. For the former, we extract a singular value as a function of ${E_T}^{\rm jet}$ by constructing the balancing distribution, as defined in Eq. 1, in bins of ${E_T}^{\rm jet}$, and fit the distribution around its peak with a Gaussian. We perform these fits separately in data and MC, and use the mean and error on the mean of the fitted Gaussian as the value of $K_{Z/\gamma}({E_T}^{\rm jet})$ and its error. We use this estimation of the most probable value in order to avoid effects from a small number of highly mismeasured jets, that will more dramatically alter the mean and median of the distribution.

The distributions of K_Z and K_γ in data and MC are shown in Fig. 1. We not only see that the jets are not well-measured (the balancing variable is non-zero), but that in the Z-jet balancing, a sample largely dominated by gluon jets, we see significant disagreement between data and MC. We do not see such disagreement in the γ-jet balancing, indicating

our MC simulation models the behavior of the jets in this sample (dominated by quark jets) well.

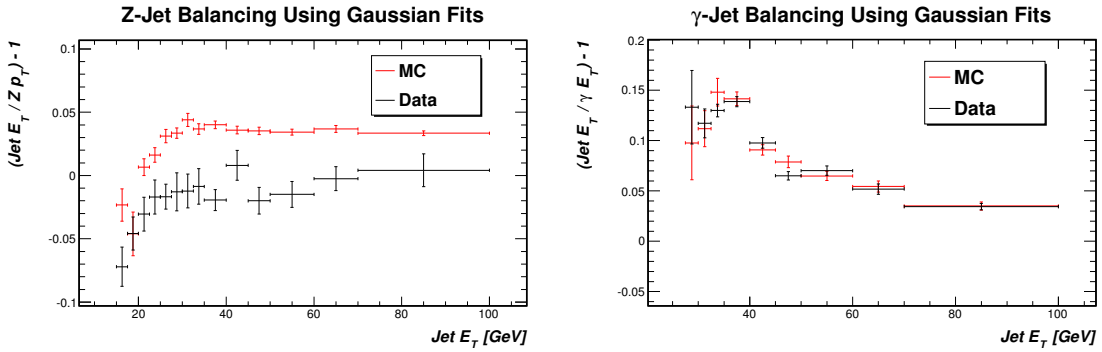

FIG. 1. The balancing distributions, K_Z (*left*) and K_γ (*right*), in data (*black*) and MC (*red*) as a function of ${E_T}^{\text{jet}}$. The uncertainties are solely the uncertainty on the mean of a Gaussian fit to the balancing distributions in bins of ${E_T}^{\text{jet}}$. We see good agreement between data and MC in the γ-jet balancing, but poor agreement in the Z-jet balancing, possibly indicating errors in our reconstruction of gluon jet energies.

The determination of $F^q_{Z/\gamma}$ in MC is fairly trivial, as we may just match jets to their originating parton. We match jets by looping through the particles in the event record, and locating the highest p_T parton located inside the cone of the jet. In our γ-jet balancing sample, we find that the quark fraction is about 85% at ${E_T}^{\text{jet}} \sim 30$ GeV, and drops to about 71% at ${E_T}^{\text{jet}} \sim 70$ GeV. In the Z-jet balancing sample, these fractions are $\sim 38\%$ and $\sim 49\%$ in the same ${E_T}^{\text{jet}}$ regions.

In data, this is not possible, and we must rely on MC simulation to extract a value of $F^q_{Z/\gamma}({E_T}^{\text{jet}})$. Because we are trying to correct for discrepancies in the reconstruction of quark and gluon jets between data and MC, we cannot simply use the MC-derived $F^q_{Z/\gamma}$ values from each jet E_T bin. Rather, in MC we parameterize $F^q_{Z/\gamma}$ as a function of $p_T^{Z/\gamma}$:

$$F^q_{Z/\gamma}{}^{\text{MC}}(p_T) = a + e^{bp_t + c}$$

and determine the $F^q_{Z/\gamma}{}^{\text{data}}$ in each jet E_T of the data based on $p_T^{Z/\gamma}$ distribution in the data.

In order to establish an uncertainty on F^q, we compare the distribution of the jet QG value (see Sec. V) in data and MC, and fit the data distribution using quark and gluon templates from the MC. We take the average deviation of this jet QG extracted value from

the nominal MC value as a systematic on F^q, constant across jet E_T. This uncertainty is $\sim 10\%$ (absolute) in both the Z-jet and γ-jet balancing samples.

Using Eqs. 4-5, we construct distributions of K_q and K_g as a function of the jet E_T, shown in Fig. 2. We see good agreement between data and MC in K_q, but worse agreement in K_g, where data appears consistently lower than MC. This suggests that MC is systematically overestimating gluon jet energies, relative to the data.

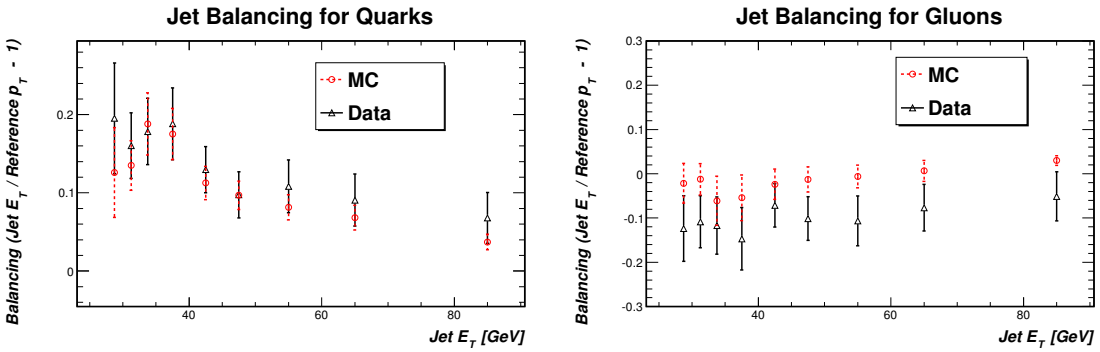

FIG. 2. The derived balancing variable for quark jets, K_q, (*left*) and gluon jets, K_g, (*right*) in data (*black*) and MC (*red*) as a function of ${E_T}^{\rm jet}$. The uncertainties on each point are from the uncertainties from the mean of the Gaussian fit and the uncertainties on the quark fractions, added in quadrature. We see better agreement between data and MC in the energy scale of quark jets than that of gluon jets, following from the behavior seen in Fig. 1.

Using the distributions of K_q and K_g, we determine the corrections that need to be applied to MC jets in order to best match the energy scale of the data. These MC corrections are defined as $({K_q}^{\rm Data}+1)/({K_q}^{\rm MC}+1)$ for quark jets, and $({K_g}^{\rm Data}+1)/({K_g}^{\rm MC}+1)$ for gluon jets, and are shown in Fig. 3. Due to the photon trigger used to select the γ-jet balancing sample, we do not have reliable balancing information for jets below 27.5 GeV in that sample, limiting the full range over which we may derive corrections. Since we are interested in jets down to energies around 20 GeV, we extrapolate to lower jet energies the quark jet energy correction derived for jets with $E_T \geq 27.5$ GeV, and use the Z-jet balancing sample to extract a gluon correction assuming this extrapolated quark correction.

Both the quark and gluon corrections appear flat in jet energy for jets with $E_T \geq 15$ GeV, and so we fit them to a constant. We find that to better match the data, quark jet energies in MC should be increased by $\sim 1.4\%$, while gluon jet energies should be decreased by $\sim 7.9\%$.

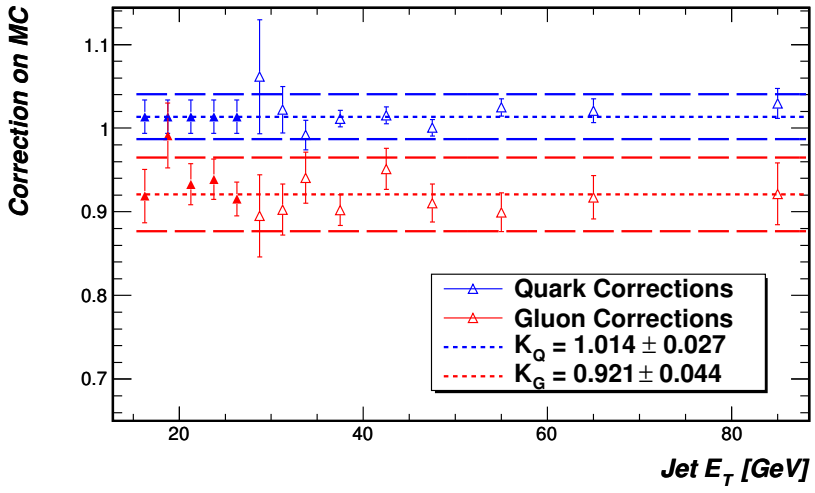

FIG. 3. The derived correction for MC quark jets (*blue*) and gluon jets (*red*) as a function of $E_T{}^{\rm jet}$. The open triangles represent corrections derived using both γ-jet and Z-jet balancing samples, while the filled triangles represent the assumed flat correction for quarks and the corresponding correction for gluons calculated from the Z-jet balancing sample alone. The error bars represent only the statistical uncertainty on the balancing variable. The short dashed lines are the fits of the correction to a constant across jet E_T, and the long dashed lines represent the total systematic error bands on that constant correction, further described in Sec. IV C.

C. Uncertainties on MC Jet Energy Corrections

We consider the following sources of error on the corrections presented in Sec. IV B.

- *Fit/Statistical Uncertainty*: We use the standard deviation of the necessary MC corrections of each jet E_T bin to capture the spread of the MC corrections around the assumed flat correction function. This is an uncertainty of $\pm 2.0\%$ for quark jet energies, and $\mp 2.5\%$ for gluon jet energies.

- F_Z^q: We vary the the quark fraction of the Z-jet sample by $\pm 10\%$ (absolute, as described in Sec. IV B), and recalculate the corrections for quark and gluon jets. This translates to an uncertainty of $\pm 0.6\%$ for quark jet energies, and $\mp 2.1\%$ for gluon jet energies.

- F_γ^q: Similarly vary the the quark fraction of the γ-jet sample by $\pm 10\%$. This translates

to an uncertainty of $\pm 1.8\%$ for quark jet energies, and $\mp 2.7\%$ for gluon jet energies.

- *Low E_T Extrapolation*: We check the dependence of the gluon jet energy corrections on the assumed quark jet corrections for low E_T jets by moving the quark jet E_T for these jets by $\pm 2\%$. We see a small change in the fit gluon energy corrections: $\mp 0.4\%$ of the jet energy.

- *Number of Interaction Vertices Dependence*: The γ-jet sample as a cut on the number of reconstructed interaction vertices to reduce contamination from pileup. The Z-jet sample does not place such a cut, in order to retain as many events as possible. We check the effect this cut has by checking for any shift in the corrections when the cut is placed on the Z-jet sample. We see a change to the quark jet energies of $\pm 0.2\%$, and the gluon jet energies of $\mp 1.2\%$.

The uncertainties are summarized in Tab. I. Because the corrections shift the energy response in MC to better match data, the quark jet and gluon jet energy correction uncertainties are anti-correlated: if the quark jet energy correction goes up, the gluon jet energy correction must go down in order to further compensate for that shift, and *vice versa*. The uncertainties are similar in magnitude to the current energy scale uncertainties [17].

		Quark jets	Gluon jets
JES Correction		1.014	0.921
Uncertainty	Fit/Statistics	0.020	0.025
	$F_Q^{Z-\text{jet}}$	0.006	0.021
	$F_Q^{\gamma-\text{jet}}$	0.018	0.027
	Low E_T Extrapolation		0.004
	N_{vert} difference	0.002	0.012
	Total	± 0.027	∓ 0.044

TABLE I. Summary of the additional jet energy corrections applied to MC jets, and the uncertainty on those corrections. The uncertainties for the quark jet and gluon jet energy corrections are anti-correlated, as they must work in concert to match the balancing distributions in data.

V. ARTIFICIAL NEURAL-NETWORK QUARK/GLUON DISCRIMINANT

In this analysis, we search for two high-p_T leptons from the decay of a Z boson, and two jets from a $W \to q\bar{q}'$ or $Z \to q\bar{q}$ decay; thus, the two jets in our signal are quark jets. Our dominant background, two jets produced in association with a $Z \to \ell^+\ell^-$ decay, contain a significant number of gluon jets. Separating quark jets from gluon jets will help increase our sensitivity to signal.

For a given energy, gluon jets, due to their higher color charge, tend to contain a higher particle multiplicity and be spatially broader in the detector than quark jets. We attempt to quantize the spatial spread of jets using a collection of artificial neural-networks (ANNs), trained to separate gluon jets from light-flavor quark jets (heavy-flavor jets tend to be more spatially spread). We call the result of the final ANN the jet Quark/Gluon value (or jet QG value). We calibrate the agreement to data of the response of the final ANN in MC using a $W \to \ell\nu+$ 1 jet sample, and determine a tagging efficiency and mistag rate of placing a cut on the jet QG value using two independent samples: $W \to \ell\nu+2$ jets, similar to our $Z+$ jets background, and $t\bar{t} \to b\bar{b}\ell\nu q\bar{q}'$, which contains two jets from the hadronic decay of a W boson.

A. Jet QG Definition

A total of three ANNs make up the final QG discriminant. There are two networks for separating quark and gluon jets by looking at the distribution of energy contained in calorimeter towers and the distribution of momenta contained in reconstructed charged-particle tracks, described in the following paragraphs. Thus, every jet may be assigned a Tower NN value and Track NN value, the output of these two ANNs. These two NN values are combined in a third ANN, along with other variables that offer some discrimination between quark and gluon jets, or that are related to the how spread or collimated jet it is.

Each of the ANNs is trained on jets matched to a light flavor quark or gluon with $p_T > 20$ GeV/$c$and within a $\Delta R = 0.4$ of the center of the jet, with no other partons above 8 GeV/$c$within a $\Delta R = 0.7$. The jets come from a $Z \to \mu^+\mu^- + 2$ parton ALPGEN sample, interfaced with PYTHIA showering. Each ANN is a feed-forward multilayer perceptron with a single output utilizing a tanh response function, implemented using the MLP algorithm

from the TMVA package [18]. The networks are trained on 100,000 quark and gluon jets, and tested for biases in over-training on a sample with 500,000 quark and gluon jets. Gluon jets are reweighted to match the E_T and η distributions of the quark jets, to remove any discrimination power coming solely from these variables.

For every jet, we obtain a list of the calorimeter towers in a cone of $\Delta R = 0.7$ around that jet. Each tower has a location coordinate, (η, ϕ), and deposited energy E associated with it. Then, for each jet, we construct a distribution of the distance, $\Delta R = \sqrt{\eta^2 + \phi^2}$, between all pairs of towers within the jet. We weight each tower pair by its relevance in terms of energy and obtain a distribution that characterizes the spatial spread of the energy within each jet. The weight we apply to each tower pair is given by:

$$\frac{E_i E_j}{0.5((\Sigma E)^2 - \Sigma E^2)}$$

where E_i and E_j are the energies of the two towers in the pair, ΣE is the sum of the energy in all towers in a cone of $\Delta R = 0.7$ around the jet, and ΣE^2 is the sum of the square of the energy of each tower in that same cone. This denominator is chosen in order to normalize the sum of all weights of tower pairs to unity. We split this distribution into 56 bins with bin size $\Delta R = 0.025$ for $0.0 \leq \Delta R \leq 1.4$, and the contents of the 53 non-zero bins (the first 3 bins are empty due to the segmentation of the calorimeter). Typical ΔR between tower pairs distributions for quark and gluon jets, with a larger bin size, are shown in Fig. 4. The output of the Tower NN for quark and gluon jets in the training/testing sample is shown in Fig. 5.

We follow a similar prescription using tracks within a cone of $\Delta R = 0/7$ around each jet, using the tracks' locations in (η, ϕ) (at the primary vertex) and momenta p to obtain a distribution of the distance between pairs of tracks (in ΔR), with each pair weighted by the momentum contained within that pair:

$$\frac{p_i p_j}{0.5((\Sigma p)^2 - \Sigma p^2)}$$

We require all tracks within the cone around the jet come from the primary vertex, and that the track $p_T > 0.4$ GeV/c. We split the ΔR distribution between track pairs into the same 56 bins as used in the Tower NN, and the content of each bin is used as an input into the Track NN. Typical ΔR between track pairs distributions for quark and gluon jets, are shown in Fig. 4. The output of the Track NN for quark and gluon jets in the training/testing sample is shown in Fig. 5.

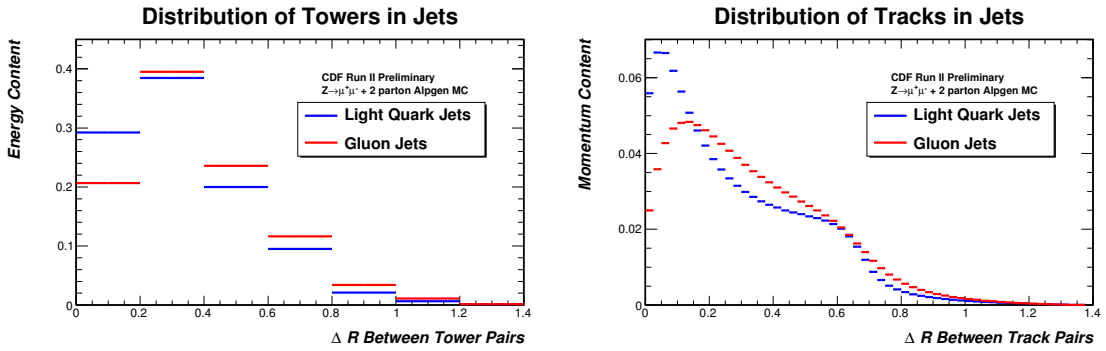

FIG. 4. Typical distributions of ΔR between pairs of towers (*left*) and between pairs of tracks (*right*) in light-flavor quark (*blue*) and gluon (*red*) jets. Light-flavor quark jets tend to peak at low ΔR, indicating they are rather collimated, while gluon jets tend to have a higher ΔR distribution. The contents of bins of these ΔR distributions are used as inputs into ANNs that discriminate between quark and gluon jets.

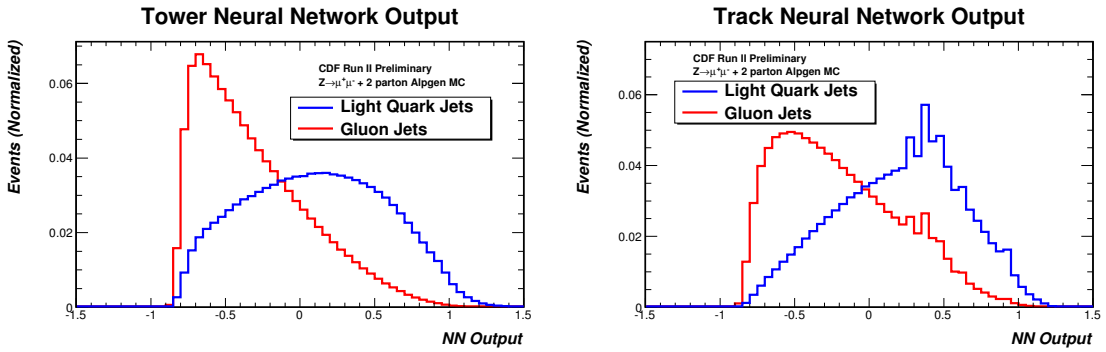

FIG. 5. The outputs of the ANNs processing tower (*left*) and track (*right*) distributions in light-flavor quark (*blue*) and gluon (*red*) jets. Higher NN scores indicate jets that are more quark-like. We see good performance in both the tower and track NNs. The spiky behavior in the track NN distribution comes from jets with only two tracks located inside a cone of $\Delta R = 0.7$, and thus have only one non-zero bin in their ΔR between track pairs distribution.

The final ANN uses the tower and track NN values as inputs, along with other jet variables that provide some discrimination power between quark jets and gluons — the ratio of ΣE in a cone of $\Delta R = 0.4$ to ΣE in a cone of $\Delta R = 0.7$, the ratio of Σp in a cone of $\Delta R = 0.4$ to Σp in a cone of $\Delta R = 0.7$, the number of towers in cones of $\Delta R = 0.4$ and 0.7, the number of tracks in cones of $\Delta R = 0.4$ and 0.7, and the jet EM fraction — and other variables

that may affect the shape of the ΔR distributions, independent of whether the jet originates from a quark or gluon — the jet E_T, the jet η, and the number of reconstructed interaction vertices. The output of this final ANN is shown in Fig. 6 for light-flavor quark and gluon jets from the training and testing samples.

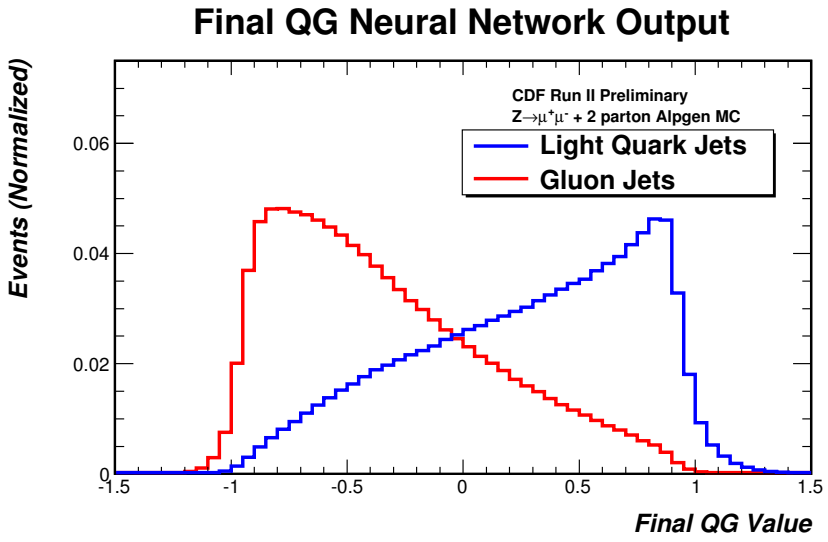

FIG. 6. The output of the final ANN for light-flavor quark (*blue*) and gluon (*red*) jets. Higher NN scores indicate jets that are more quark-like. In MC jets, we see good separation between quark and gluon jets.

B. Jet QG Calibration and Cut Efficiency/Mistag Rate

The response of the ANN quark/gluon discriminant may differ between data and MC simulation, especially since raw (uncorrected) tower energies are used in the construction of the tower ANN, as CDF does not employ individual tower energy corrections. Since our signal and most backgrounds are modeled with MC, it is necessary to calibrate the Monte Carlo response to match the behavior of the data. We do so using an independent control region with jets similar to those in our final state – $W \rightarrow \ell\nu +$ 1 jet events – and then further validate and establish uncertainties on the modeling using data regions very similar to our signal and dominant background regions: $t\bar{t}$ decays in lepton + jets final states, and $W \rightarrow \ell\nu + 2$ jet events, respectively.

To form our $W + 1$ jet calibration sample, we choose data come from standard high-p_T central electron or muon triggers, requiring there be one and only one central lepton of high quality with $p_T > 20$ GeV/c. To pick events consistent with a $W \to \ell\nu$ decay, we also require a large amount of missing transverse energy, $\not\!\!E_T > 25$ GeV, and a reconstructed transverse mass consistent with leptonic W decays, $m_T > 25$ GeV/c^2. To further eliminate any contributions from multijet events where a jet "fakes" our lepton $+\not\!\!E_T$ signature, we require that the $\not\!\!E_T$ not be aligned with any reconstructed jet ($\Delta\phi(\not\!\!E_T$,jet) > 0.2 radians), and that the $\not\!\!E_T$-significance (as defined in [5]) be larger than 1 for events with muons, and larger than 4 for events with electrons. We require that the events in this calibration sample have one jet with $E_T > 20$ GeV and $|\eta| \leq 2.0$, but no other jet above 20 GeV.

We consider a number of processes that may contribute to this selection, and model them with a combination of PYTHIA, ALPGEN, and MADGRAPH [19] event generators interfaced with PYTHIA for showering. The dominant contribution is $W \to \ell\nu$ production in association with one jet, which we model using an ALGPEN event generator interfaced with PYTHIA for showering, similar to our $Z+$ jets MC sample. As we are largely concerned with the agreement in shapes between data and MC, we scale the MC to match the normalization of the data. Additionally, we reweight the MC to match the jet E_T and η distribution of the data, to remove these variables as a factor in any mismodeling of the other quantities used in forming the jet QG value.

We see mismodeling in the Tower NN values, where the data appears more gluon-like than the MC. Jets in data appearing more spatially spread than jets in MC is consistent with the disagreements between data and MC in jet energies, describe in Sec. IV: the amount of energy contained within a cone of $\Delta R = 0.4$ is higher in MC gluon jets than those in data. We correct for these discrepancies using a linear shift in of the Tower NN values in MC in order to match the data in the $W + 1$ jet sample. We perform different linear shifts for jets in the central and plug calorimeters, and for jets in events with different levels of pileup. After making this calibrations in the MC Tower NN values, we make further corrections to the response of the final ANN to better match the correlations of these calibrated Tower NN values with other jet quantities: the number of towers in the jets, and the ratio of ΣE in a cone of $\Delta R = 0.4$ to ΣE in a cone of $\Delta R = 0.7$. We see a smaller level of mismodeling in the Track NN, and introduce a similar linear shift in MC Track NN values to better match data. The calibrated variables are input directly into the final ANN, without retraining the

network.

We further validate the response of the jet QG value by comparing data and MC simulation in $W \to \ell\nu + 2$ jets sample and in a sample of $t\bar{t}$ where two quark jets originate from the hadronic decay of a W boson. Tab. II summarizes the cuts placed to form these two samples: the $W + 2$ jet sample is similar to the previously described $W + 1$ jet sample, except we modify the cuts on the jets to match those used in the signal region of our $ZW/ZZ \to \ell\ell jj$ search. The $t\bar{t}$ selection eschews the $\not\!\!E_T$-sig and m_T cuts to reduce multijet backgrounds in favor of requiring a minimum scalar sum of the E_T of identified objects (jets, $\not\!\!E_T$, and the lepton p_T) in the event. Because we are interested in selecting the two jets in the $t\bar{t}$ selection that come from the decay of a W, and are not b-jets from a $t \to Wb$ decay, we make use of the jet $b$ness tagger, described in [20]. We classify the two jets with the highest $b$ness score as the two b-jets, and the remaining two jets as those coming from a $W \to q\bar{q}'$ decay.

W + Jets Selection	$t\bar{t}$ Selection
central e or μ, $p_T > 20$ GeV/c	
$\not\!\!E_{T\,L5} > 25$ GeV	
$\Delta\phi(\not\!\!E_T$,Nearest Jet) > 0.4 rad	$\Delta\phi(\not\!\!E_T$,Nearest Jet) > 0.2 rad
$\not\!\!E_T$-sig > 4 (e only)	
$W m_T > 25$ GeV/c^2(e only)	
	Sum $E_T > 300$ GeV
$N_{jets}(E_T > 20$ GeV$) = 2$	$N_{jets}(E_T > 20$ GeV$) = 4$
	2^{nd} highest $b$ness jet > -0.5
$1^{\text{st}}/2^{\text{nd}}$ jet $E_T > 25$ GeV	2 highest $b$ness jets $E_T > 20$ GeV
	2 lowest $b$ness jets $E_T > 25$ GeV
Jets' $\lvert\eta\rvert < 2.0$	
ΔR between jets > 0.7	

TABLE II. Summary of event selection requirements for our $t\bar{t}$ lepton + jets selection and our W + 2 jets selection, used to understand the modeling of events in our QG discriminant. Cuts in the center are shared cuts in the two samples. See the text for descriptions of "Sum E_T" and "jet $b$ness".

Because we are looking for jet QG shape differences between data and MC that will

translate to acceptance uncertainties when we place a cut on the jet QG value, we scale the number of $W+$ jet events in the MC to match the data in our $W+2$ jets sample. The number of events in each sample is shown in Tab. III. The distributions of the maximum and minimum QG values of the two jets considered are shown in Fig. 7. We see fairly good modeling in the $t\bar{t}$ sample, while poorer modeling in the $W+2$ jet sample, where after our calibrations, the jets in MC is slightly more gluon-like than the jets in data.

	W + Jets Events	$t\bar{t}$ Events
W + jets*	21520 ± 2150	38.7 ± 3.9
W + b jets*	937 ± 375	13.8 ± 5.5
Z/DY + jets	1249 ± 125	3.1 ± 0.3
Z/DY + b jets	86 ± 34	1.4 ± 0.6
WW/WZ	1386 ± 83	5.9 ± 0.4
$t\bar{t}$	2145 ± 129	469 ± 28.1
$t\bar{t}$ (b-jets)		108 ± 6.5
$t\bar{t}$ (q-jets)		361 ± 21.7
Total Expected	27319*	544
Data	27319	579

TABLE III. The number of events in the W + 2 jets and $t\bar{t}$ lepton + jets region, showing only the uncertainties assigned on the normalization of each sample. The * refers to samples whose normalizations are modified in order to agree with data, as explained in the text. The distinction between b and q jets in the $t\bar{t}$ sample refers to the lower two $b$ness jets: events where both jets are matched to non-b quark jets are labeled "q-jets", while if one of the jets is matched to a b jet, it is labeled "b-jets".

We find maximum sensitivity to our signal when forming a "light-flavor tagged" channel by requiring the minimum jet QG value of the jets in our analysis be > 0.0. We determine an efficiency for quarks to pass this cuts, and gluons to be "mistagged" using this cut, with the $t\bar{t}$ and $W+2$ jet samples in the following way. The efficiency measured in data – $e_D(q)$, as it is a function of the QG cut placed – may be expressed as:

$$e_D(q) = \frac{e_{raw}(q) - s_m(q) m_{MC}(q) f_g}{1 - f_g} \tag{6}$$

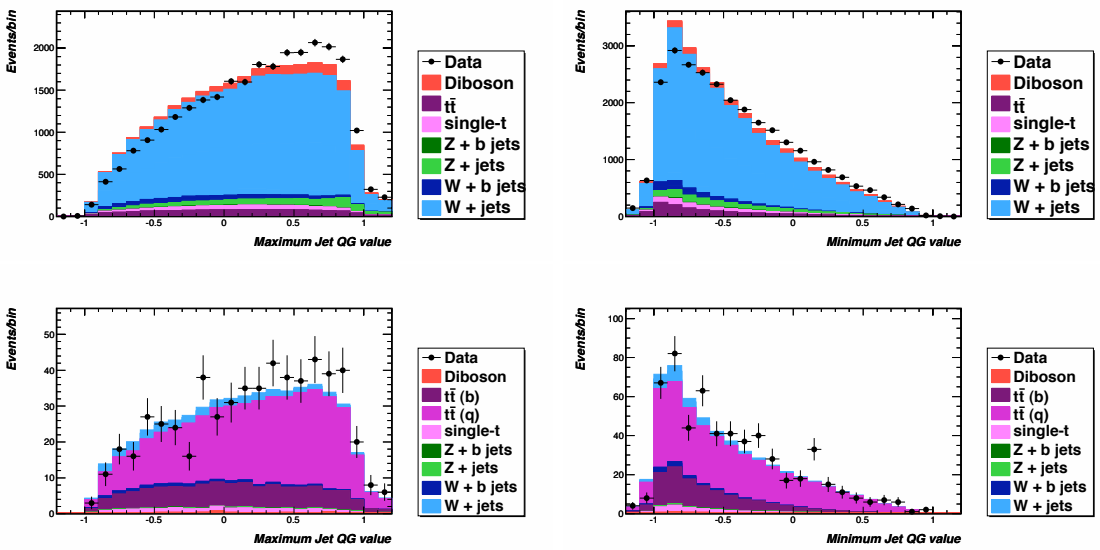

FIG. 7. Distribution of the maximum (*left*) and minimum (*right*) jet QG values of the two jets in our $W + 2$ jet (*top*) and $t\bar{t}$ (*bottom*) samples. The distinction between b and q jets in the $t\bar{t}$ sample refers to the lower two $b$ness jets: events where both jets are matched to non-b quark jets are labeled "q-jets", while if one of the jets is matched to a b jet, it is labeled "b-jets".

where e_{raw} is the fraction of data events passing the QG cut; m_{MC} is the mistag rate for gluons to pass the cut, as measured in MC; s_m is a scale factor on the mistag rate in MC to match the mistag rate measured in data; and, f_g is the fraction of gluon jets in the sample. We can write a similar expression for getting the mistag rate from:

$$m_D(q) = \frac{m_{raw}(q) - s_e(q)e_{MC}(q)f_q}{1 - f_q} \tag{7}$$

where m_{raw} is the fraction of data events passing the QG cut; e_{MC} is the efficiency for quarks to pass the cut, as measured in MC; s_e is a scale factor on the efficiency in MC to match the mistag rate measured in data; and, f_q is the fraction of quark jets in the sample. Uncertainties on these quantiites may be expressed like so:

$$\begin{aligned}\sigma_e^2(b) = &\frac{1}{(1-f_g)^2}\left(\frac{e_{\rm raw}(1-e_{\rm raw})}{N_D} + (\sigma_m f_g)^2\right) \\ &+ \sum_X \frac{\sigma_X^2}{\left[N_{\rm MC}(1-f_g)\right]^2} \times \\ &\left[(e+s_m m)(f_g - f_g^X) + f_q^X(e_{\rm MC} - e_X)\right]^2\end{aligned} \tag{8}$$

where N_D and N_{MC} are the number of data and MC events, and where the X represents

the various subsamples of the MC. A similar expression exists for the mistag rate. The uncertainty here includes a statistical uncertainty on the data, uncertainties on the mistag rate and efficiency, and uncertainties on the relative difference in the contributions from the MC. We take the uncertainties on the normalizations of our $t\bar{t}$, single-t, diboson, W/Z + jets, and $W/Z + b$ jets to be 6%, 10%, 6%, 10%, and 40%, respectively.

We measure the efficiency in the $t\bar{t}$ sample, where we have a very small number of gluon jets, and measure the mistag rate in the $W + 2$ jets sample, where the gluon fraction is much larger, and similar to our $Z + 2$ jet signal region. The efficiency and mistag rate and their uncertainties are determined using an iterative procedure, as they rely on one-another. We see fast convergence on the final measurements of the efficiency and mistag rate. Tab. IV shows the efficiency and mistag rate for our given cut at minimum QG > 0.0, measured in both data and MC. We see that the MC underestimates the rate for quark jets to pass the jet QG cut, while correctly predicting the observed mistag rate.

	MC	Data	MC Eq. Cut (-1σ,Nom.,$+1\sigma$)
Efficiency	0.241	0.295 ± 0.034	$(-0.0325, -0.09, -0.14)$
Mistag Rate	0.088	0.087 ± 0.027	$(0.09, -0.0175, -0.11)$

TABLE IV. The efficiency and mistag rates for our QG cuts, as evaluated in data and MC, along with the necessary cut value changes in MC to model the proper rates and the uncertainties on them.

We implement a correction to the MC by shifting the cut on the minimum QG value in order to match the efficiency/mistag rate of the data. The uncertainties on these quantities are also implemented using this shift in cut, allowing us to have both rate and shape uncertainties due to the QG tag requirement. The shifted cut values used for MC quark and gluon jets are listed in Tab. IV.

VI. SIGNAL EXTRACTION AND RESULTS

We extract the number of signal events using a binned χ^2-minimization fit to data, using methods described in [21]. We supply histogram templates for our signal and background

samples. The templates, along with the uncertainties we assign to their normalization in the fit procedure, are listed below:

- ZW/ZZ signal: We allow the normalization of the signal template to float unconstrained in the fit. We assume each signal process contributes proportionally to its predicted SM cross section: 3.6 pb for ZW and 1.5 pb for ZZ [1].

- Z + jets: This is our largest background, and we also allow its normalization to float in the fit, unconstrained.

- $Z + b$ jets: A significant background when placed b-tags on jets, we constrain this template's normalization to be within 40% of the Z + jets normalization.

- $t\bar{t}$: We assign an uncertainty of 6.5%, based on the theoretical cross section uncertainty [22], on the normalization of this template.

- Fakes: We use the method described in Sec. III to construct templates for the contribution from jets faking one or two leptons. We assign an uncertainty of 50% on the fake rate, based on studies using different trigger thresholds in the jet data used to obtain the fake rates.

We perform a simultaneous fit to data using these templates in three channels. For events passing the basic signal selection requirements described in Sec. III, we first construct a heavy-flavor tag (HF-tag) channel composed of events passing a minimum jet $b$ness requirement, using the jet $b$ness tagger described in [20]. For events failing this requirement, we then pick events passing the minimum jet QG value requirement described in Sec. V to form a light-flavor tag (LF-tag) channel. Events failing this requirement are then placed in the third "untagged" channel, which has a lower signal fraction than the two tagged channels, but still has a significant amount of signal due to the tight placement of the tagging requirements.

Additional systematic uncertainties on both the normalization and shapes of the templates used in the fit are also considered. We consider uncertainties due to mismodeling between data and MC simulation in the jet energy scale (as described in Sec. IV C) and the jet energy resolution, the modeling of the tagging variables, and the lepton energy scale and resolution. Additional shape uncertainties on the Z + jets backgrounds are considered

Systematics in Fit	channel	WZ and ZZ	Z + jets	$Z + b$ jets	$t\bar{t}$	Fakes
σ/Norm.	all	*unconstr.*	*unconstr.*	±40%	±6.5%	±50%
Jet Resolution	HF-Tag	±0.8%	±0.3%	±1.0%	±0.2%	
	LF-Tag	±1.0%	±0.7%	±1.5%	±6.2%	
	No-Tag	±0.6%	±0.9%	±0.7%	±1.1%	
Jet Energy Scale	HF-Tag	±4.0%	±4.4%	±3.8%	±4.0%	
	LF-Tag	±1.5%	±0.3%	±0.6%	±3.0%	
	No-Tag	±1.9%	±5.7%	±3.8%	1.9%	
Q^2	all		shape only	shape only		
ISR/FSR	all	shape only				
*b*ness Tag	HF-Tag	±7.8%	±7.8%	±9.2%	±7.6%	
	LF-Tag	±0.2%	±0.0%	±1.2%	±2.8%	
	No-Tag	±0.4%	±0.1%	±1.8%	±4.5%	
QG Tag	LF-Tag	±10%	±16%	±2.0%	±15%	
	No-Tag	±4.3%	±3.5%	±2.0%	±2.0%	
Lepton Energy Scale	all	±0.5%	±0.5%	±0.5%	±1.5%	
Lepton Energy Res.	all	±0.1%	±0.1%	±0.0%	±2.7%	

TABLE V. Summary of the systematic uncertainties considered in the fit of the dijet mass distribution. Uncertainties that change both the shape and rate of templates used in the fit are treated in a correlated fashion.

by varying the primary interaction's momentum transfer, Q^2, up and down by a factor of two. We also consider the effect increasing or decreasing initial and final state radiation has on our extracted signal. These systematic uncertainties, along with the normalization constraints for certain templates described above, are treated as nuisance parameters in the fit, and included in the χ^2-minimization procedure (see [21]). They are summarized in Tab. V.

Fig. 8 shows the result of the fit to signal, and the number of events fit for in each template are summarized in Tab. VI. We fit for $\approx 50\%$ of the expected signal normalization, and see good agreement between data and MC in the final fit in each of the three fitting channels, with a total χ^2/d.o.f= 59.8/55.

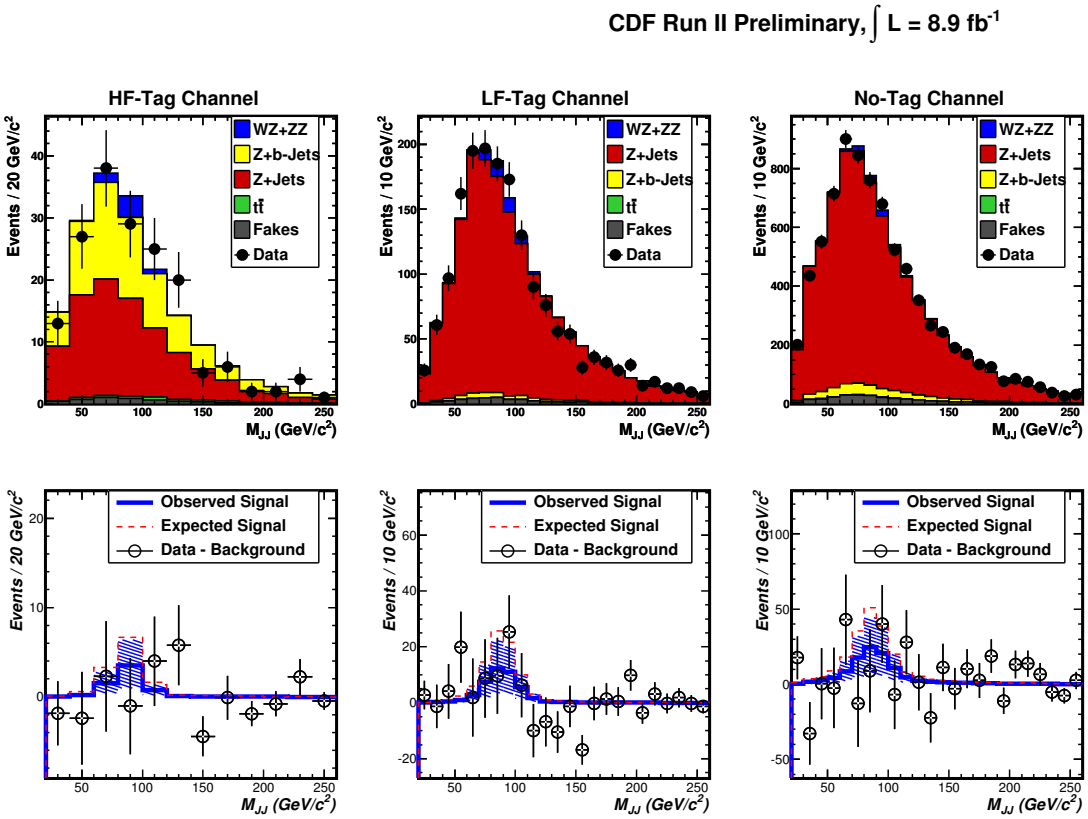

FIG. 8. Result of the fit to data for ZW/ZZ in our dilepton + dijet selection in our HF-tag channel (*left*), HF-tag channel (*center*), and untagged channel (*right*). The top row shows the output from the fit compared to the data, while the bottom row shows the background subtracted from data, compared to the expected (*red dashed line*) and fitted (*blue solid line, with uncertainties in blue bands*) signal contributions.

We establish bounds and limits on the cross section of ZW/ZZ production using a Feldman-Cousins method [23], where we analyze the distribution of measured cross sections in pseudo-experiments generated with a variety of scale factors on the input signal cross section. When generating pseudo-experiments, we consider additional systematic uncertainties that affect our acceptance, assigning a 2% uncertainty from parton distribution functions to the signal MC template, and 2.5% and 6% uncertainties on all MC templates due to the lepton scale factor determination and luminosity, respectively. The set of input cross sections in our pseudo-experiments range from 0.0 to 2.9 times the expected cross section, with a step size of 0.1.

Process N_{events}, HF-Tag N_{events}, LF-Tag N_{events}, No-Tag			
Z + jets	91.9 ± 8.3	1605 ± 50	7200 ± 600
$Z + b$ jets	71 ± 14	37 ± 10	360 ± 100
$t\bar{t}$	3.18 ± 0.35	0.71 ± 0.07	5.26 ± 0.42
Fakes	4.6 ± 2.3	39 ± 20	270 ± 140
Total Bkg.	171 ± 14	1681 ± 36	7840 ± 600
$ZW + ZZ$	6.3 ± 4.4	45 ± 30	106 ± 72
Total Events	177 ± 14	1726 ± 40	7940 ± 610
Data Events	172	1724	7950

TABLE VI. The number of events in each fitting channel from our best fit to the data.

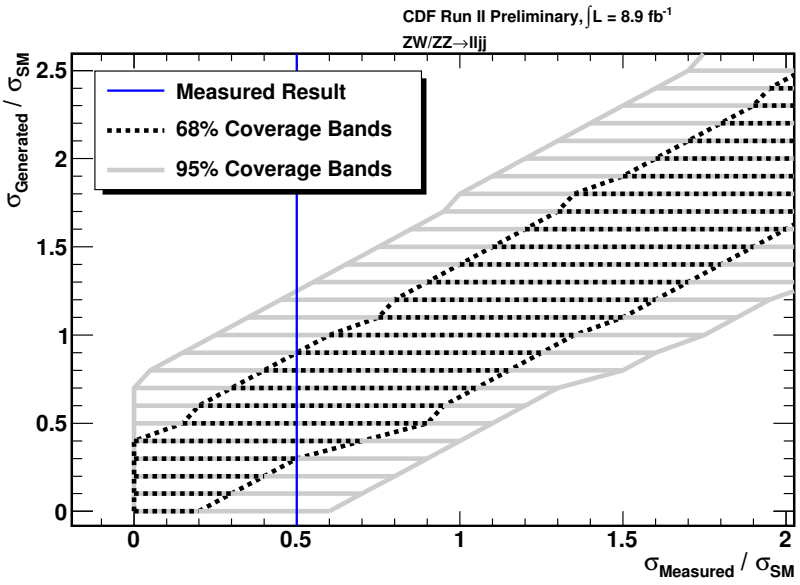

FIG. 9. Condence bands showing the expected range of measured cross sections as a function of the true cross section, with 68% CL (black dashed region) and 95% CL (solid gray region). Our measured result of $\sigma(p\bar{p} \rightarrow ZW/ZZ) = 2.5^{+2.0}_{-1.0}$ pb corresponds to a limit of $\sigma_{ZW/ZZ} < 6.35$ pb $(1.25 \times \sigma_{SM})$ at the 95% C.L.

Fig. 9 shows the results of our Feldman-Cousins analysis. Using the 1σ bands, we measure $\sigma(p\bar{p} \rightarrow ZW/ZZ) = 2.5^{+2.0}_{-1.0}$ pb, compared to the standard model prediction of $\sigma_{SM} = 5.08$ pb. We do not exclude the no-signal hypothesis, and establish a limit of $\sigma_{ZW/ZZ} <$

6.35 pb ($1.25 \times \sigma_{SM}$) at the 95% C.L.

ACKNOWLEDGMENTS

We thank the Fermilab staff and the technical staffs of the participating institutions for their vital contributions. This work was supported by the U.S. Department of Energy and National Science Foundation; the Italian Istituto Nazionale di Fisica Nucleare; the Ministry of Education, Culture, Sports, Science and Technology of Japan; the Natural Sciences and Engineering Research Council of Canada; the National Science Council of the Republic of China; the Swiss National Science Foundation; the A.P. Sloan Foundation; the Bundesministerium für Bildung und Forschung, Germany; the Korean World Class University Program, the National Research Foundation of Korea; the Science and Technology Facilities Council and the Royal Society, UK; the Institut National de Physique Nucleaire et Physique des Particules/CNRS; the Russian Foundation for Basic Research; the Ministerio de Ciencia e Innovación, and Programa Consolider-Ingenio 2010, Spain; the Slovak R&D Agency; the Academy of Finland; and the Australian Research Council (ARC).

[1] J. M. Campbell and R. K. Ellis, Phys. Rev. D **60**, 113006 (1999)

[2] K. Hagiwara *et al.*, Nucl. Phys. **B 282**, 253 (1987)

[3] M. Kober, B. Koch, and M. Bleicher, Phys. Rev. D **76**, 125001 (2007)

[4] E. J. Eichten, K. Lane, and A. Martin, Phys. Rev. Lett. **106**, 251803 (Jun 2011)

[5] T. Aaltonen *et al.* (CDF Collaboration), Phys. Rev. Lett. **103**, 091803 (2009)

[6] T. Aaltonen *et al.* (CDF Collaboration), Phys. Rev. Lett. **104**, 101801 (2010)

[7] T. Aaltonen *et al.* (CDF Collaboration), Phys. Rev. Lett. **106**, 171801 (Apr 2011)

[8] V. M. Abazov *et al.* (D0 Collaboration), Phys. Rev. Lett. **108**, 181803 (May 2012)

[9] T. Aaltonen *et al.* (CDF Collaboration), Phys. Rev. D **85**, 012002 (Jan 2012)

[10] A. Abulencia *et al.* (CDF Collaboration), J. Phys. G **34**, 2457 (2007)

[11] The coordinate system used to describe the detector has its origin located at the detector's center. The proton beam direction is defined as the $+z$ direction. The polar angle, θ, is measured from the origin with respect to the z axis, and ϕ is the azimuthal angle. Pseudorapidity, transverse energy, and transverse momentum are defined as $\eta{=}-\ln\tan(\theta/2)$, $E_T{=}E\sin\theta$, and $p_T{=}p\sin\theta$, respectively. The rectangular coordinates x and y point radially outward and vertically upward from the Tevatron ring, respectively.

[12] F. Abe *et al.* (CDF Collaboration), Phys. Rev. D **45**, 1448 (1992)

[13] We define the missing transverse momentum $\vec{\not\!\!E}_T \equiv -\sum_i E^i_{\rm T}\mathbf{n}_i$, where $\mathbf{n}_i$ is the unit vector in the azimuthal plane that points from the beamline to the ith calorimeter tower. We call the magnitude of this vector $\not\!\!E_T$

[14] M. L. Mangano *et al.*, J. High Energy Phys. **07**, 001 (2003)

[15] T. Sjöstrand *et al.*, J. High Energy Phys. **05**, 026 (2006)

[16] T. Aaltonen *et al.* (CDF Collaboration), Phys. Rev. D **79**, 052008 (2009)

[17] A. Bhatti *et al.*, Nucl. Instrum. Methods A **566**, 375 (2006)

[18] A. Hoecker, P. Speckmayer, J. Stelzer, J. Therhaag, E. von Toerne, and H. Voss, PoS **ACAT**, 040 (2007), arXiv:physics/0703039

[19] J. Alwall *et al.*, J. High Energy Phys. **09**, 028 (2007)

[20] J. Freeman *et al.*, Nuclear Instruments and Methods in Physics Research Section A: Accelerators, Spectrometers, Detectors and Associated Equipment **663**, 37 (2012)

[21] T. Aaltonen *et al.* (CDF Collaboration), Phys. Rev. D **82**, 112005 (2010)

[22] U. Langenfeld, S. Moch, and P. Uwer, Phys. Rev. D **80**, 054009 (2009)

[23] G. J. Feldman and R. D. Cousins, Phys. Rev. D **57**, 3873 (1998)